Search for resonances in the 65 to 110 GeV diphoton invariant mass range using $80\,\text{fb}^{-1}$ of pp collisions collected at $\sqrt{s} = 13\,\text{TeV}$ with the ATLAS detector

The ATLAS Collaboration

A search for low-mass diphoton resonances is performed using $80\,\text{fb}^{-1}$ of pp collision data collected with the ATLAS detector at the Large Hadron Collider. Pairs of isolated photon candidates with high transverse momentum are selected, probing the diphoton invariant mass spectrum in the range 65 to 110 GeV. No significant excess with respect to the Standard Model expectation is found, and a limit at the 95% confidence level is set on narrow resonance fiducial cross-section times branching ratio ranging from 30 to 101 fb.

1 Introduction

New resonances decaying into two photons are predicted in many extensions of the Standard Model (SM) [1–5]. The diphoton final state has the advantage of a clean experimental signature with an excellent mass resolution and moderate background. This note focuses on the search for a narrow resonance X of mass m_X in the low-mass range 65 to 110 GeV, below the SM Higgs boson mass of 125 GeV [6, 7].

This range exhibits two peculiarities compared to searches at higher diphoton invariant masses. First, in addition to the smoothly falling continuum background composed of photon pairs ($\gamma\gamma$), as well as photon–jet (γj) and jet pairs (jj) with mis-identified jets, a Drell-Yan (DY) component is present. This DY contribution originates from $Z/\gamma^* \to e^+e^-$ decays, where the electrons are both reconstructed as photons (hereafter indicated as $e \to \gamma$). Due to the large bremsstrahlung that these electrons typically undergo, the reconstructed invariant mass $m_{\gamma\gamma}$ of this background exhibits a shape that peaks below the Z boson mass. Hence, a careful evaluation of both the shape and magnitude of this background is required. Furthermore, selecting photon candidates with transverse energy close to the trigger threshold sculpts the diphoton invariant mass spectrum at its lower edge, an effect that must be accurately described by the background model.

A model composed of analytic functions that describe the signal and background (including $\gamma\gamma$, γj, jj and DY) is fit to the measured diphoton mass spectrum to search for narrow resonances. The shape and normalization of the function describing the DY background is constrained using a data-driven measurement of $e \to \gamma$ events in $Z \to ee$ decays. Events are split into three categories depending on how the two photon candidates are reconstructed: both unconverted (UU), one converted and one unconverted (CU) or both converted (CC). This categorization improves the sensitivity of the search since the DY contamination is more prominent in the CC category, and less prominent in the UU category. The fit is performed within the range $60 < m_{\gamma\gamma} < 120$ GeV, in order to quantify the presence of a potential signal and set a limit on a signal fiducial cross-section times branching ratio $\mathcal{B}(X \to \gamma\gamma)$ in the range $65 < m_X < 110$ GeV.

Previous low-mass diphoton search results were obtained by the ATLAS Collaboration with data collected at 8 TeV [8]. The CMS Collaboration observed a small excess near 95 GeV with a local (global) significance of 2.8 (1.3) standard deviations when combining data recorded at 8 TeV and 13 TeV [9].

2 Data and Simulated Samples

The ATLAS detector [10, 11] was used to collect $\sqrt{s} = 13$ TeV proton–proton (pp) collisions from the 2015–2017 Large Hadron Collider (LHC) running periods, corresponding to an integrated luminosity of (80.4 ± 1.6) fb^{-1}. The uncertainty is derived, following a methodology similar to that detailed in Ref. [12], from calibrations of the luminosity scale using x–y beam-separation scans performed in August 2015, May 2016 and July 2017 (the results for 2017 are still preliminary). The data were recorded using diphoton triggers that required two electromagnetic clusters with transverse energies E_T[1] above a certain threshold,

---

[1] ATLAS uses a right-handed coordinate system with its origin at the nominal interaction point (IP) in the center of the detector and the z-axis along the beam pipe. The x-axis points from the IP to the center of the LHC ring, and the y-axis points upwards. Cylindrical coordinates (r, ϕ) are used in the transverse plane, ϕ being the azimuthal angle around the z-axis. The pseudorapidity is defined in terms of the polar angle θ as $\eta = -\ln\tan(\theta/2)$. Angular distance is measured in units of $\Delta R \equiv \sqrt{(\Delta\eta)^2 + (\Delta\phi)^2}$.

as well as satisfying identification criteria based on variables describing the shape of the electromagnetic showers in the calorimeter (hereafter called "shower shapes"). In 2015 and the first portion of 2016, the E_T threshold was 20 GeV, while in the remainder of 2016 $E_T > 22$ GeV was required. During 2017, the E_T threshold was reverted to 20 GeV, however an additional requirement on calorimeter isolation transverse energy was applied.

Simulated event samples are used to study signal and background processes, as well as to determine the analytic functions used to model both. The search itself is performed by using the data to determine the parameters of the analytic function used to model the background (see Section 5). Interference effects between the resonant signal and background processes are neglected.

Background events containing two photons with associated jets are simulated with the SHERPA 2.2.4 [13] event generator. Matrix elements are calculated with up to 3 partons at next-to-leading order (NLO) in quantum chromodynamics (QCD) [14], and merged with the SHERPA parton shower [15] according to the ME+PS@NLO prescription [16]. Events containing a photon with associated jets are simulated with the SHERPA 2.1.1 event generator. Matrix elements are calculated with up to 4 partons at leading order (LO) in QCD and merged with the SHERPA parton shower according to the ME+PS@LO prescription [17]. For both SHERPA samples, the CT10 parton distribution function (PDF) set [18] is used in conjunction with dedicated parton shower tuning developed by the SHERPA authors. Events containing both one and two photons are also simulated with the PYTHIA 8.186 [19–21] event generator at LO in QCD, for comparison with SHERPA. Here, the A14 set of tuned parameters for the underlying event [22] is used together with the NNPDF2.3LO PDF set [23]. Events containing Z bosons are generated at NLO in QCD using POWHEG-BOX v2 [24, 25] interfaced to the PYTHIA 8.186 parton shower model and the CT10 PDF set is used. The AZNLO set of tuned parameters for the underlying event [26] is used, with PDF set CTEQ6L1.

The nominal signal samples, corresponding to the gluon–gluon fusion production mode (ggF), were generated using the effective-field-theory approach implemented in MADGRAPH5_aMC@NLO version 2.3.3 [27] at NLO in QCD. Samples were generated with the NNPDF3.0 NLO PDF set [28], using the A14 set of tuned parameters of PYTHIA 8.186 for the parton-shower and hadronization simulation. Alternative samples were generated at NLO in QCD using POWHEG-BOX v2 interfaced to the PYTHIA 8.186 parton shower model using the AZNLO set of tuned parameters, for the gluon fusion and vector-boson fusion production modes. Samples were also simulated with the PYTHIA 8.186 event generator using the A14 set of tuned parameters, assuming the production of a Higgs boson in association with a W, Z or top-quark pair. Simulated samples were produced for fixed values of the mass of the assumed resonance, spanning the range 60 to 200 GeV. All assume a narrow-width resonance of 4 MeV that is negligible compared to the experimental resolution, ranging from 1.4 to 1.8 GeV (see Section 4).

The background events containing two photons were processed through a fast detector simulation based on a parameterization of the performance of the calorimeters [29]. All other generated events were propagated through a full detector simulation based on GEANT 4 [30], except for multiple overlaid pp collisions, which are soft QCD processes simulated with PYTHIA 8.186 using the A2 set of tuned parameters [31] and the MSTW2008LO PDF set [32]. The simulated events are weighted to reproduce the distribution of average number of individual pp interactions per bunch crossing, as well as the distribution of the primary vertex z-position, observed in data.

3 Event Selection

Photon candidates are reconstructed from clusters of energy deposited in the electromagnetic calorimeter, as well as from charged-particle tracks and conversion vertices reconstructed in the inner detector. The event reconstruction is similar to the one described in Ref. [33], with the exception of the photon cluster definition: instead of a fixed-size sliding window, an algorithm based on topological clusters is used [34, 35].

Photons are required to fall within the pseudorapidity interval $|\eta| < 2.37$, excluding the transition region $1.37 < |\eta| < 1.52$ between the barrel and end-cap calorimeters. The energy calibration is based on a multivariate regression algorithm [36] optimized on simulated samples [35] and used to determine corrections to the energy of the clusters. The two candidates with the highest transverse energies, both satisfying $E_T > 22\,\text{GeV}$, are retained. This transverse energy requirement is slightly higher than the trigger threshold, for most of the data taking periods, to mitigate the efficiency turn-on effect. These photon candidates are used to select the diphoton vertex using a neural-network algorithm based on charged-particle tracks and primary vertex information, as well as the direction of the two photons measured in the calorimeters and inner tracker. The diphoton vertex is used to redefine the direction of the photon candidates, resulting in an improved $m_{\gamma\gamma}$ resolution.

The photons must also fulfill identification criteria based on the shower shapes in the electromagnetic calorimeter [37]. Small differences in the average values of the shower shape variables between data and simulation are corrected in the simulation. The efficiency of the photon identification increases with E_T from 70% at 20 GeV to 90% at 50 GeV.

To improve the rejection of jets misidentified as photons, the candidates are required to be isolated using both calorimeter and tracking detector information. The calorimeter-based isolation variable E_T^{iso} is defined as the scalar sum of the E_T over positive-energy topological clusters within a radius $\Delta R = 0.2$ around the photon candidate, excluding the photon energy and correcting for pile-up and underlying-event contributions [38–40]. For both candidates this variable is required to be below $0.065 \cdot E_T$, where E_T is the transverse energy of the photon. The isolation variable p_T^{iso} is based on charged-particle tracks, and is defined as the scalar sum of the transverse momenta p_T over tracks within a radius $\Delta R = 0.2$ around the photon candidate. Only tracks with transverse momentum $p_T > 1\,\text{GeV}$ that are consistent with originating from the diphoton production vertex and that are not associated with a photon conversion vertex are used. For both candidates this variable is required to be below $0.05 \cdot E_T$. Small differences in the average value of E_T^{iso} between data and simulation are corrected in the simulation. The combined isolation efficiency for photons fulfilling the identification requirement in simulated signal samples increases with $m_{\gamma\gamma}$ from 80% at 60 GeV to 90% at 120 GeV.

Finally, only events with a measured diphoton invariant mass in the range $60 < m_{\gamma\gamma} < 120\,\text{GeV}$ are considered. After applying the full selection, four significant background components are identified: $\gamma\gamma$, γj and jj pairs coming from QCD production, as well as *ee* pairs coming from DY production. The contribution of the SM Higgs boson is found to be negligible. To evaluate the background composition and the fraction of irreducible diphoton events (including fake photons coming from DY electrons), the 2x2D sideband method described in Ref. [41] is used. This method is based on signal and background enriched control regions defined from data sidebands, built by inverting the photon identification and isolation criteria. The signal leakage in the background control regions is evaluated with simulation. The results of this background decomposition are shown in Table 1. The diphoton purity increases with the invariant mass $m_{\gamma\gamma}$ and varies from 60 % to 70 % across the 60 to 120 GeV range. The uncertainties on

this purity measurement arise from statistical uncertainty in the data and simulated samples, the definition of the control regions, the dependence of the signal leakage evaluation in the control regions on the event generator, the modeling of the isolation and shower-shape distributions, and a possible correlation between the identification and isolation criteria. The background composition result is used to build the background template for the background model validation (see Section 5).

4 Signal Modelling

The signal, assumed to have a narrow decay width relative to the mass resolution, is modeled by a double-sided Crystal Ball (DSCB) function, composed of a Gaussian core with power-law tails [42, 43]. Each parameter is determined in a fit to the fixed-mass simulated samples, and is parametrized as a function of m_X separately for each conversion category. The width of the Gaussian core, which is entirely determined by detector resolution, ranges from 1.4 to 1.8 GeV. Good agreement between the signal model and the simulated $m_{\gamma\gamma}$ distribution is found, as shown in Figure 1 for the UU category. The photon energy calibration (resolution) results in an uncertainty in the signal mass scale (resolution) of ±0.3 to 0.5% (±2 to 8%), with larger uncertainty at higher values of $m_{\gamma\gamma}$.

5 Background Estimate

The two main components of the background, the non-resonant continuum and the resonant DY, are estimated separately in each category. In both cases, a data-driven approach is used to describe the normalization and shape of the background processes. The continuum is fitted on data, with the normalization and function parameters free, while for the DY both shape and normalization are fitted but constrained.

Table 1: The number of events recorded in data N_{data}, the number of expected Drell-Yan events $N_{\text{DY}}^{\text{exp}}$ derived from data as explained in Section 5, and the relative fraction f of $\gamma\gamma$, γj, jγ and jj components determined with the 2x2D sideband method in each photon conversion category. In this table the distinction is made for photon–jet pairs when the photon is the leading (γj) or subleading (jγ) p_T candidate. The uncertainties correspond to the quadratic sum of statistical and systematic uncertainties.

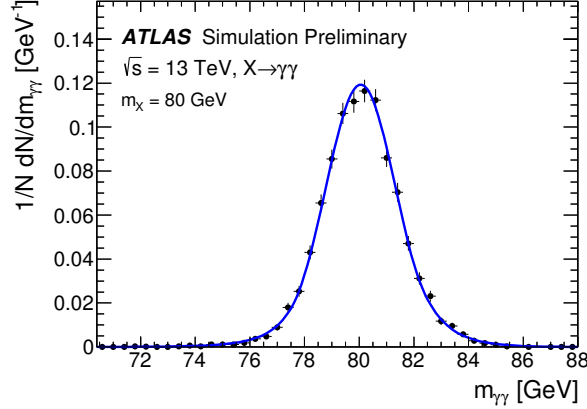| Category	UU	CU	CC
N_{data}	1204889	1025072	234166
$N_{\text{DY}}^{\text{exp}}$	5000 ± 1100	18800 ± 2000	22300 ± 2600
$f_{\gamma\gamma}$	$0.688^{+0.021}_{-0.048}$	$0.661^{+0.029}_{-0.034}$	$0.654^{+0.045}_{-0.027}$
$f_{\gamma\text{j}}$	$0.175^{+0.037}_{-0.026}$	$0.181^{+0.029}_{-0.025}$	$0.179^{+0.051}_{-0.044}$
$f_{\text{j}\gamma}$	$0.080^{+0.027}_{-0.017}$	$0.093^{+0.031}_{-0.025}$	$0.093^{+0.035}_{-0.048}$
f_{jj}	$0.057^{+0.023}_{-0.028}$	$0.065^{+0.029}_{-0.034}$	$0.074^{+0.043}_{-0.050}$

Figure 1: Simulated diphoton invariant mass distribution of a narrow-width signal particle X of mass 80 GeV (points) in the UU category, overlaid with the double-sided Crystal Ball function resulting from the signal model parametrization (line).

The continuum background is predominately composed of events from $\gamma\gamma$ but also γj and jj production processes. It is described by an analytic function whose form and uncertainty are determined using the method described in Ref. [44]. The size of the maximal *spurious signal* in the range 65 to 110 GeV extracted by a signal-plus-background fit to a background-only template is considered, and the analytic function with the smallest value is selected. The background only template is built using simulated samples for the $\gamma\gamma$ component and a data control sample for the γj and jj components, mixed according to the fractions presented in Section 3. The following functions are considered: a Fermi–Dirac distribution, Bernstein polynomials of order five to seven, a Landau distribution and the sum of a Landau distribution with an exponential distribution. The Landau and Fermi–Dirac functions are considered in order to model the kinematic turn on around 60 GeV. The sum of a Landau distribution with an exponential distribution is used for the UU and CU categories and the size of the spurious signal is 604 and 496 events, respectively. A fifth-order Bernstein polynomial is used for the CC category, with a spurious signal of 181 events. The size of this spurious signal relative to its uncertainty corresponds to 128%, 104% and 79% for the UU, CU and CC categories respectively. Since more data events have been collected than in Ref. [33], the background template—limited in precision by available simulated samples—has larger statistical fluctuations compared to the observed statistical precision of the data. For this reason the relaxed criteria described in Ref. [44] is used, leading to a relatively high spurious-signal uncertainty.

The DY background is modeled using a DSCB function, with parameters determined by fitting a template derived from simulated events. Due to the limited size of the simulated $Z/\gamma^* \rightarrow ee$ sample where both electrons are reconstructed as photons, the shape of the background is determined using a fit to a dielectron data sample. Because electrons faking a photon generally lose a large amount of energy due to bremsstrahlung, a Smirnov transformation [45] derived from simulation is used to correct the dielectron template shape. The normalization of the resulting template is computed from $e \rightarrow \gamma$ fake rates in data, as described in Ref. [8]. A comparison of the contribution from simulated fake electrons (denoted $\gamma\gamma$) with the transformation of the simulated dielectron template (denoted $ee \rightarrow \gamma\gamma$) is shown in Figure 2 for the UU and CC categories, where good agreement is observed. Since electrons reconstructed as unconverted photons are more affected by bremsstrahlung than those reconstructed as converted photons, the UU events are more shifted to lower invariant masses than CC events. Uncertainties in the peak position (± 0.1 to 0.2%), the template shape (± 2 to 3%) and normalization (± 9 to 21%) are considered, as illustrated in

Appendix A.

A background-only fit of the data is shown in Figure 3, for each of the three conversion categories. As expected, the DY contribution is most prominent in the CC category.
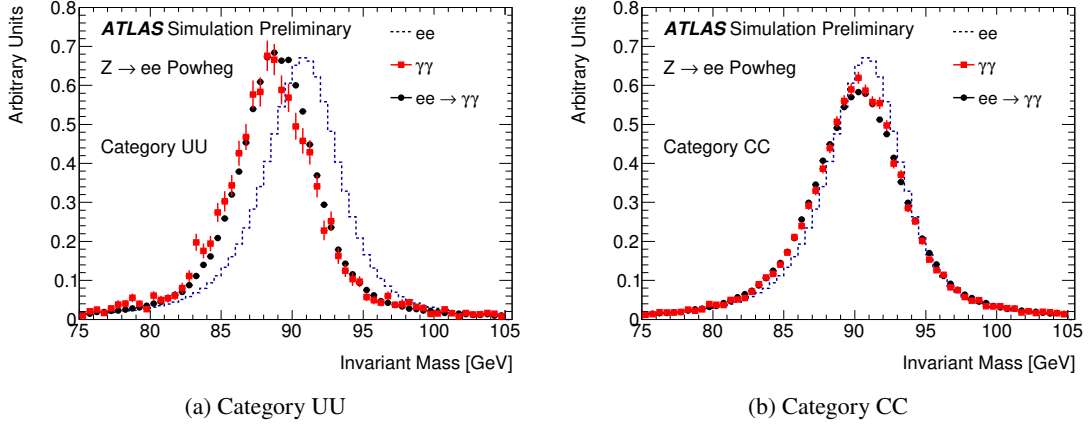

(a) Category UU

(b) Category CC

Figure 2: Invariant mass distributions in the (a) UU and (b) CC categories for fully simulated $Z \rightarrow ee$ events reconstructed as ee (black dotted-lines), reconstructed as $\gamma\gamma$ (red squares), and reconstructed as ee after applying the Smirnov transform (black circles).

6 Results

The measurement of the signal production cross-section times branching ratio ($\sigma_{\text{fid}} \cdot \mathcal{B}$) is performed in a fiducial region defined at the particle level as: two photons with $E_{\text{T}} > 22\,\text{GeV}$, $|\eta| < 2.37$ excluding $1.37 < |\eta| < 1.52$ and passing the isolation requirement $E_{\text{T}}^{\text{iso}} < 0.065\,E_{\text{T}}$. Here, $E_{\text{T}}^{\text{iso}}$ is defined as the scalar sum of p_{T} for all particles with lifetime longer than $10\,\text{ps}$ (except neutrinos and muons) within a radius $\Delta R = 0.2$ around the photon. This isolation requirement is chosen to reproduce the detector-level selection. The acceptance, defined as the probability of an event to be in the fiducial volume at the particle level, varies from 22 to 55% depending on the mass and on the production process, as discussed in Appendix B.

The particle-level fiducial cross-section includes a signal efficiency correction factor C_X through:

$$\sigma_{\text{fid}} \cdot \mathcal{B} = \frac{N_{\text{S}}}{C_X \mathcal{L}}, \text{ with } C_X = \frac{N_{\text{MC}}^{\text{det}}}{N_{\text{MC}}^{\text{fid}}}, \tag{1}$$

where N_{S} is the fitted number of signal events in data, $\mathcal{L}$ is the integrated luminosity, $N_{\text{MC}}^{\text{det}}$ is the number of simulated events passing the detector-level selection criteria and $N_{\text{MC}}^{\text{fid}}$ is the number of simulated events passing the particle-level selection. The fiducial region is defined in order to reduce the dependence of C_X on the chosen theoretical model. This model dependence is checked using simulated samples of X with several production modes: gluon–gluon fusion, vector boson fusion, production associated with a vector boson and production associated with top–antitop quark pairs. The C_X factor is parametrized using the ggF sample for the nominal value, and ranges from 0.46 to 0.69 as a function of m_X. This parametrization is shown in Appendix B. The envelope of the C_X values from the five production modes is taken as an
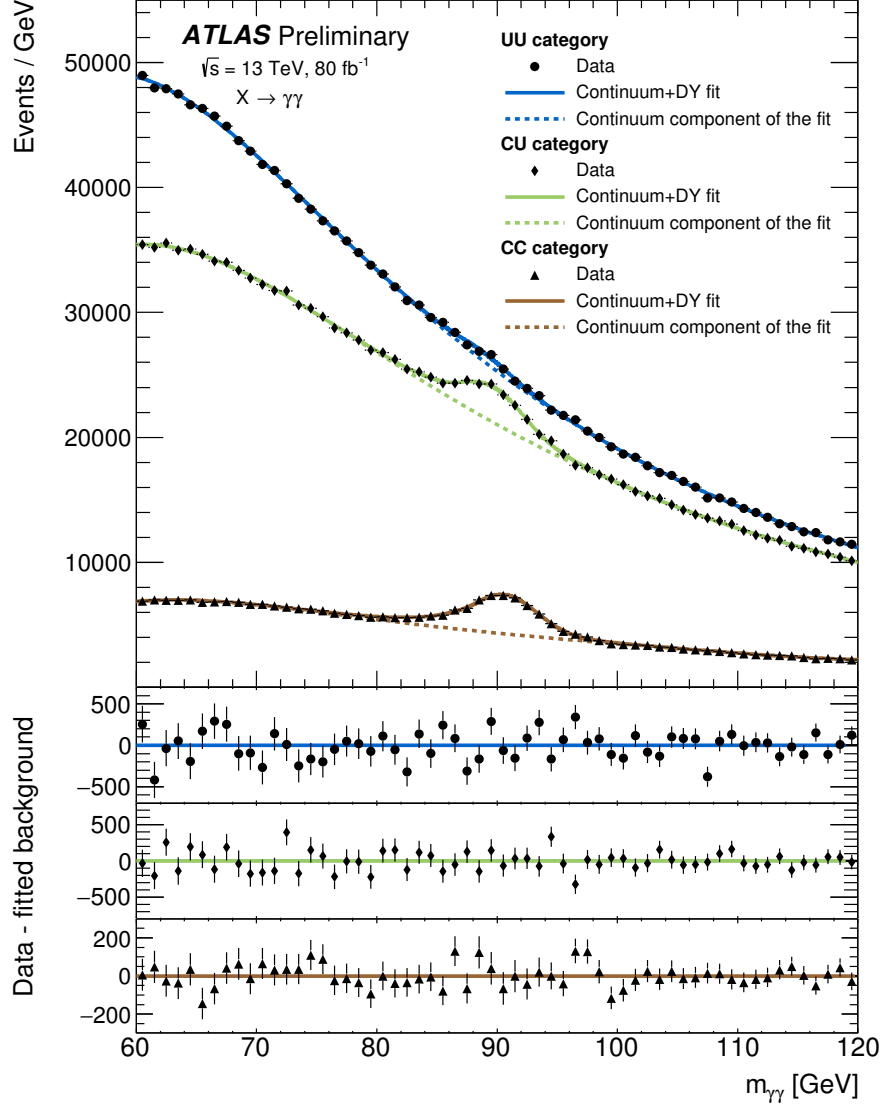
Figure 3: Background-only fit to the data (black markers) as a function of the diphoton invariant mass $m_{\gamma\gamma}$ for the three conversion categories. The solid lines show the sum of the Drell-Yan and the continuum background components, the dashed lines show only the continuum background components. The difference between the data and the total background component is shown at the bottom separately for each category.

uncertainty. The uncertainty in the simulation of the trigger and multiple pp interactions occurring in the same bunch crossing (pileup) is also considered, as well as photon identification, isolation, energy calibration, and energy resolution. The magnitude of these uncertainty components is shown in Table 2.

The expected fraction of signal events in each of the three conversion categories is parameterized as a function of m_X. A systematic uncertainty is derived from the variation of the detector material description in the simulation, resulting in migrations across categories. Differences in category fractions between the signal production modes are found to be negligible.

The number of signal and background events is measured with an extended maximum-likelihood fit to the $m_{\gamma\gamma}$ spectra in the three conversion categories. A scan over different m_X hypotheses is performed in the range 65 to 110 GeV.

The signal-plus-background model has the form:

$$N_{\text{S}} \cdot f_{\text{S}}(m_{\gamma\gamma}) + N_{\text{spur}} \cdot f_{\text{S}}(m_{\gamma\gamma}) + N_{\text{B}} \cdot f_{\text{B}}(m_{\gamma\gamma}) + N_{\text{DY}} \cdot f_{\text{DY}}(m_{\gamma\gamma}) \tag{2}$$

where f_{S} is the signal probability density function (*pdf*) described in Section 4, N_{S} (N_{B}) is the fitted number of signal (continuum background) events and f_{B} (f_{DY}) is the continuum (Drell-Yan) background model described in Section 5. The systematic uncertainties are included in the likelihood via nuisance parameters, and constrained by Gaussian or log-normal penalty terms. Their values are summarized in Table 2. N_{spur} is the number of spurious signal events and N_{DY} is the number of DY background events, both constrained by their uncertainties (see Section 5).

The compatibility of the observed diphoton mass spectra with the background-only hypothesis, for a given signal hypothesis X, is determined with a local p-value based on the profile-likelihood-ratio-test statistic [46] as detailed in Ref. [43]. The observed and expected 95% confidence level (CL) exclusion limits on the fiducial cross-section times branching ratio are evaluated using a modified frequentist approach CL_{s} [47] with the asymptotic approximation to the test-statistic distribution [46].

The result of the p-value scan is shown in Figure 4(a), where no significant excess with respect to the background-only hypothesis is observed. An upper limit at the 95% CL is set on $\sigma_{\text{fid}} \cdot \mathcal{B}$ from 30 to 101 fb in the range $65 < m_{\gamma\gamma} < 110$ GeV, as shown in Figure 4(b). The dominant uncertainties correspond to the background modeling and the limited number of pp collisions recorded, which are comparable in magnitude. The impact of the systematic uncertainties on the expected limit is shown in Appendix C.
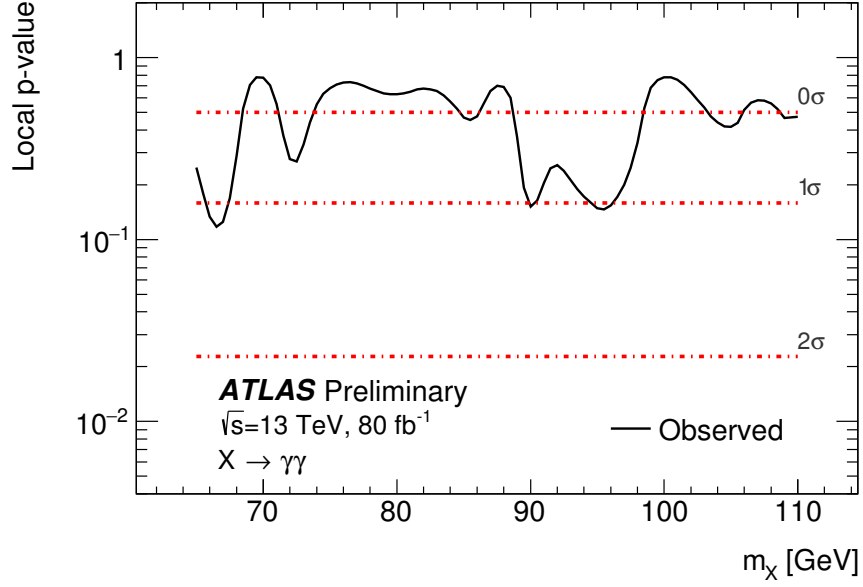
(a)
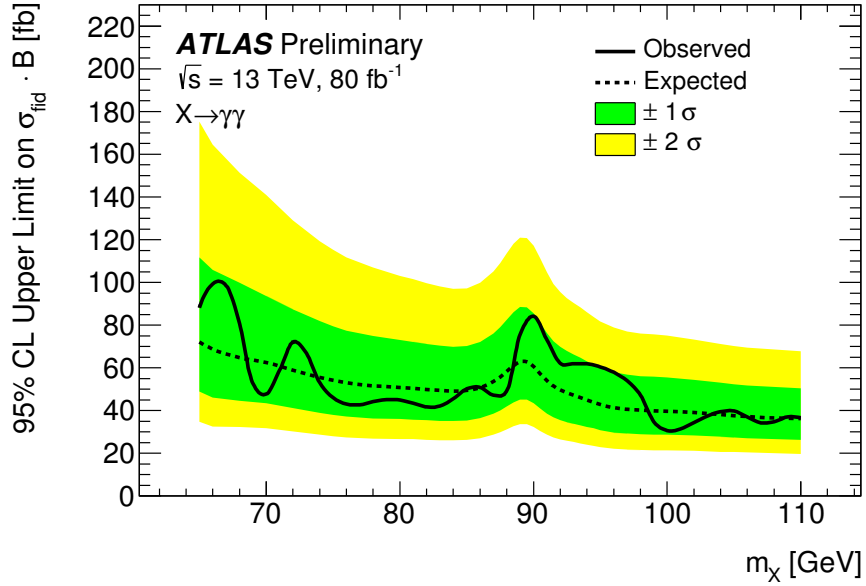
(b)

Figure 4: The (a) compatibility, in terms of local *p*-value (solid line), with the background-only hypothesis as a function of the assumed signal mass m_X, the dotted-dashed lines correspond to the standard deviation quantification σ; and the (b) upper limit on the fiducial cross-section times branching ratio $\mathcal{B}(X \rightarrow \gamma\gamma)$ as a function of m_X, where the solid (dashed) line corresponds to the observed (expected) limit and the green (yellow) band corresponds to one (two) standard deviation from the expectation.

Table 2: Summary of the systematic uncertainties on the expected event yield. The values correspond to the uncertainties associated to the fit nuisance parameters.

Source	Uncertainty [%]	Remarks
Signal yield		
Luminosity	± 2	
Trigger eff.	$\pm 1.4 - 1.7$	m_X-dependent
Photon identification eff.	$\pm 1.5 - 2.3$	m_X-dependent
Isolation eff.	± 4	
Photon energy scale	$\pm 0.13 - 0.49$	m_X-dependent
Photon energy resolution	$\pm 0.053 - 0.28$	m_X-dependent
Pile-up	$\pm 1.8 - 4.1$	m_X-dependent
Production mode	$\pm 2.4 - 25$	m_X-dependent
Signal modeling		
Photon energy scale	$\pm 0.3 - 0.5$	m_X- and category–dependent
Photon energy resolution	$\pm 2 - 8$	m_X- and category-dependent
Migration between categories		
Material	$-2.0 / +1.0 / +4.1$	category-dependent (UU/CU/CC)
Non-resonant Background		
Spurious Signal	128 / 104 / 79	ratio to the expected spurious signal uncertainty
	(604 / 496 / 181 events)	(category-dependent)
DY Background modeling		
Peak position	$\pm 0.1 - 0.2$	category-dependent
Peak width	$\pm 2 - 3$	category-dependent
Normalization	$\pm 9 - 21$	category-dependent

7 Conclusion

A search for Higgs-like narrow-width resonances is performed in the diphoton invariant mass spectra ranging from 65 to 110 GeV, using 80 fb^{-1} of pp collision data collected at $\sqrt{s} = 13$ TeV with the ATLAS detector at the Large Hadron Collider. The dominant uncertainties arise from the limited number of pp collisions collected and the uncertainty due to the choice of analytic functions to model the continuum background. No significant excess above the SM expectation is observed and limits are set on the fiducial cross-section times branching ratio in a fiducial region defined to mimic the detector-level selection. Cross-sections above 30 to 101 fb are excluded at the 95% CL, depending on the diphoton invariant mass.

Appendix

A Drell-Yan background template

The Drell-Yan background template used in the fit for the CC category is shown in Fig. 5, along with its variations coming from the systematic uncertainties on the normalization, the width and position of the peak.
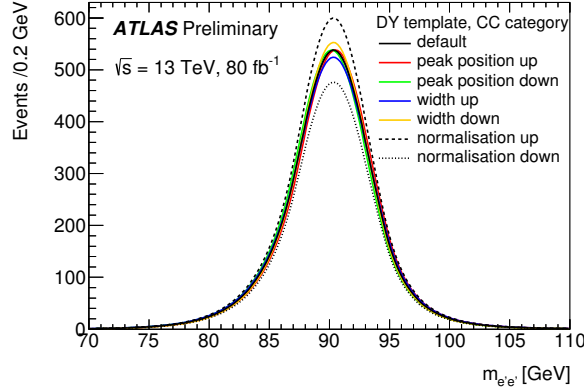

Figure 5: Data-driven template of the Drell-Yan background for the CC category, built from reconstructed ee candidates Smirnov transform into diphoton candidates $e'e'$. The black solid line corresponds to the default template and the others correspond to the systematic variations of the normalization, width and position of the Z peak.

B Acceptance and efficiency correction factors

The acceptance A_X and efficiency correction C_X factors are defined as

$$A_X = \frac{N_{\text{MC}}^{\text{fid}}}{N_{\text{MC}}^{\text{tot}}}, \text{ and } C_X = \frac{N_{\text{MC}}^{\text{det}}}{N_{\text{MC}}^{\text{fid}}}, \tag{3}$$

where $N_{\text{MC}}^{\text{fid}}$ is the number of simulated events passing the particle-level selection, $N_{\text{MC}}^{\text{tot}}$ is the total number of simulated events and $N_{\text{MC}}^{\text{det}}$ is the number of simulated events passing the detector-level selection criteria. The expected number of signal events in the fiducial region $N_{\text{S}}^{\text{exp}}$ can then be expressed as $N_{\text{S}}^{\text{exp}} = \mathcal{L}\sigma\mathcal{B}(X \rightarrow \gamma\gamma)A_X C_X$, where σ is the signal production cross-section, related to the fiducial cross-section by $\sigma_{\text{fid}} = A_X\sigma$. The acceptance and the correction factors as functions of the signal mass are shown in Fig. 6(a) and 6(b), for several production modes. Values obtained with gluon–gluon fusion are used as reference and the dashed black lines correspond to the resulting parametrization of A_X and C_X. The A_X one can be expressed as

$$A_X(m_X) = 0.57 - 2.07 \, e^{-3.13 \, m_X/100}, \tag{4}$$

with m_X in GeV.

Compared to gluon–gluon fusion ggF, the vector boson fusion VBF and associated production with top quarks pair ttH have larger A_X because they have on average photons with larger p_T. Modes of associated production with vector boson W/ZH have lower A_X values because they generate photons with larger η. The photon isolation and identification efficiencies increase with the photon p_T. That is why A_X and C_X factors increase with m_X (for A_X only the isolation plays a role). Also for this reasons the alternative production modes VBF, W/ZH and ttH, that have on average photons with larger p_T, have higher C_X values than ggF. The maximal difference is observed at 60 GeV and is around 30%, of which approximately 20% is due to the difference in photon identification efficiency and 10% due to the difference in isolation efficiency.
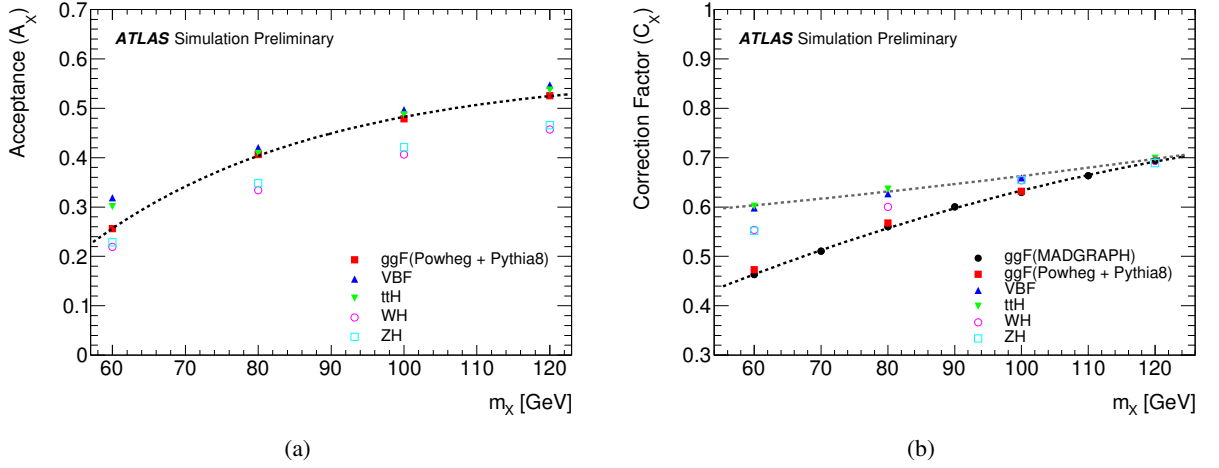

Figure 6: In (a) the acceptance (A_X) in the fiducial volume as a function of the assumed signal mass m_X for different production modes, the dashed line represents the acceptance parametrization of the nominal gluon–gluon fusion mode; and in (b) the efficiency correction factor (C_X) as a function of m_X for different production modes, the dashed black line represents the parametrization of the nominal gluon–gluon fusion mode and the dashed gray line represents the parametrization of the maximal deviation from the nominal values.

C Systematic uncertainties impact

The impact of the systematic uncertainties on the expected 95% CL upper limit on the fiducial cross-section times branching ratio is illustrated in Figure 7. The spurious signal uncertainty, corresponding to the systematic uncertainty on the continuum background modeling, is dominant. In addition, the sensitivity loss around 90 GeV corresponds to the effect of the uncertainty on the DY background description.
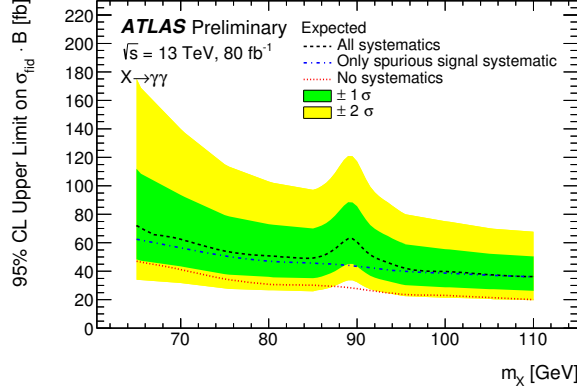
Figure 7: Expected upper limit on the fiducial cross-section times branching ratio $\mathcal{B}(X \to \gamma\gamma)$ as a function of m_X, with all the systematic uncertainties considered (black), only the spurious signal systematic uncertainty (blue) and without systematic uncertainties (red).

References

[1] M. J. G. Veltman and F. J. Yndurain, *Radiative correction to WW scattering*, Nucl. Phys. B **325** (1989) 1.

[2] R. Schabinger and J. D. Wells, *A minimal spontaneously broken hidden sector and its impact on Higgs boson physics at the CERN Large Hadron Collider*, Phys. Rev. D **72** (2005) 093007, arXiv: `hep-ph/0509209`.

[3] B. Patt and F. Wilczek, *Higgs-field portal into hidden sectors*, (2006), arXiv: `hep-ph/0605188`.

[4] T. D. Lee, *A theory of spontaneous T violation*, Phys. Rev. D **8** (1973) 1226.

[5] A. Mariotti, D. Redigolo, F. Sala, and K. Tobioka, *New LHC bound on low-mass diphoton resonances*, (2017), arXiv: `1710.01743 [hep-ph]`.

[6] ATLAS and CMS Collaborations, *Combined Measurement of the Higgs Boson Mass in pp Collisions at $\sqrt{s}$ = 7 and 8 TeV with the ATLAS and CMS Experiments*, Phys. Rev. Lett. **114** (2015) 191803, arXiv: `1503.07589 [hep-ex]`.

[7] ATLAS Collaboration, *Measurement of the Higgs boson mass in the $H \to ZZ^* \to 4\ell$ and $H \to \gamma\gamma$ channels with $\sqrt{s}$ = 13 TeV pp collisions using the ATLAS detector*, (2018), arXiv: `1806.00242 [hep-ex]`.

[8] ATLAS Collaboration, *Search for Scalar Diphoton Resonances in the Mass Range 65–600 GeV with the ATLAS Detector in pp Collision Data at $\sqrt{s}$ = 8 TeV*, Phys. Rev. Lett. **113** (2014) 171801, arXiv: `1407.6583 [hep-ex]`.

[9] *Search for new resonances in the diphoton final state in the mass range between 70 and 110 GeV in pp collisions at $\sqrt{s}$ = 8 and 13 TeV*, tech. rep. CMS-PAS-HIG-17-013, CERN, 2017, URL: `https://cds.cern.ch/record/2285326`.

[10] ATLAS Collaboration, *The ATLAS Experiment at the CERN Large Hadron Collider*, JINST **3** (2008) S08003.

[11] ATLAS Collaboration, *ATLAS Insertable B-Layer Technical Design Report*, CERN-LHCC-2010-013, 2010, URL: `https://cds.cern.ch/record/1291633`.

14

[12] ATLAS Collaboration,
Luminosity determination in pp collisions at $\sqrt{s}$ = 8 TeV using the ATLAS detector at the LHC,
Eur. Phys. J. C **76** (2016) 653, arXiv: 1608.03953 [hep-ex].

[13] T. Gleisberg, S. Höche, F. Krauss, M. Schönherr, S. Schumann, et al.,
Event generation with SHERPA 1.1, JHEP **02** (2009) 007, arXiv: 0811.4622 [hep-ph].

[14] F. Siegert, *A practical guide to event generation for prompt photon production with Sherpa*,
J. Phys. **G44** (2017) 044007, arXiv: 1611.07226 [hep-ph].

[15] S. Schumann and F. Krauss,
A Parton shower algorithm based on Catani-Seymour dipole factorisation, JHEP **03** (2008) 038,
arXiv: 0709.1027 [hep-ph].

[16] S. Höche, F. Krauss, M. Schönherr, and F. Siegert,
QCD matrix elements + parton showers: The NLO case, JHEP **04** (2013) 027,
arXiv: 1207.5030 [hep-ph].

[17] S. Höche, F. Krauss, S. Schumann, and F. Siegert, *QCD matrix elements and truncated showers*,
JHEP **05** (2009) 053, arXiv: 0903.1219 [hep-ph].

[18] H.-L. Lai et al., *New parton distributions for collider physics*, Phys. Rev. **D82** (2010) 074024,
arXiv: 1007.2241 [hep-ph].

[19] T. Sjöstrand et al., *An Introduction to PYTHIA 8.2*, Comput. Phys. Commun. **191** (2015) 159,
arXiv: 1410.3012 [hep-ph].

[20] T. Sjöstrand, S. Mrenna, and P. Z. Skands, *PYTHIA 6.4 Physics and Manual*, JHEP **05** (2006) 026,
arXiv: hep-ph/0603175.

[21] T. Sjöstrand, S. Mrenna, and P. Z. Skands, *A Brief Introduction to PYTHIA 8.1*,
Comput. Phys. Commun. **178** (2008) 852, arXiv: 0710.3820 [hep-ph].

[22] ATLAS Collaboration, *ATLAS Pythia 8 tunes to 7 TeV data*, ATL-PHYS-PUB-2014-021, 2014,
URL: https://cdsweb.cern.ch/record/1966419.

[23] R. D. Ball et al., *Parton distributions with LHC data*, Nucl. Phys. B **867** (2013) 244,
arXiv: 1207.1303 [hep-ph].

[24] S. Alioli, P. Nason, C. Oleari, and E. Re, *A general framework for implementing NLO calculations
in shower Monte Carlo programs: the POWHEG BOX*, JHEP **06** (2010) 043,
arXiv: 1002.2581 [hep-ph].

[25] S. Alioli, P. Nason, C. Oleari, and E. Re,
NLO vector-boson production matched with shower in POWHEG, JHEP **07** (2008) 060,
arXiv: 0805.4802 [hep-ph].

[26] ATLAS Collaboration, *Measurement of the Z/γ^* boson transverse momentum distribution in pp
collisions at $\sqrt{s}$ = 7 TeV with the ATLAS detector*, JHEP **09** (2014) 55,
arXiv: 1406.3660 [hep-ex].

[27] J. Alwall et al., *The automated computation of tree-level and next-to-leading order differential
cross sections, and their matching to parton shower simulations*, JHEP **07** (2014) 079,
arXiv: 1405.0301 [hep-ph].

[28] R. D. Ball et al., *Parton distributions for the LHC Run II*, JHEP **04** (2015) 040,
arXiv: 1410.8849 [hep-ph].

[29] ATLAS Collaboration,
The simulation principle and performance of the ATLAS fast calorimeter simulation FastCaloSim,
ATL-PHYS-PUB-2010-013, 2010, URL: https://cds.cern.ch/record/1300517.

[30] S. Agostinelli et al., *GEANT4: A Simulation toolkit*, Nucl. Instrum. Meth. A **506** (2003) 250.

[31] ATLAS Collaboration, *Summary of ATLAS Pythia 8 tunes*, ATL-PHYS-PUB-2012-003, 2012,
URL: https://cds.cern.ch/record/1474107.

[32] A. D. Martin, W. J. Stirling, R. S. Thorne, and G. Watt, *Parton distributions for the LHC*,
Eur. Phys. J. **C63** (2009) 189, arXiv: 0901.0002 [hep-ph].

[33] ATLAS Collaboration, *Search for new phenomena in high-mass diphoton final states using
37 fb^{-1} of proton–proton collisions collected at $\sqrt{s}$ = 13 TeV with the ATLAS detector*,
Phys. Lett. B **775** (2017) 105, arXiv: 1707.04147 [hep-ex].

[34] ATLAS Collaboration,
Topological cell clustering in the ATLAS calorimeters and its performance in LHC Run 1,
Eur. Phys. J. C **77** (2017) 490, arXiv: 1603.02934 [hep-ex].

[35] ATLAS Collaboration, *Electron and photon reconstruction and performance in ATLAS using a
dynamical, topological cell clustering-based approach*, ATL-PHYS-PUB-2017-022, 2017,
URL: https://cds.cern.ch/record/2298955.

[36] ATLAS Collaboration,
Electron and photon energy calibration with the ATLAS detector using LHC Run 1 data,
Eur. Phys. J. C **74** (2014) 3071, arXiv: 1407.5063 [hep-ex].

[37] ATLAS Collaboration, *Photon identification in 2015 ATLAS data*, ATL-PHYS-PUB-2016-014,
2016, URL: https://cds.cern.ch/record/2203125.

[38] ATLAS Collaboration, *Measurement of the inclusive isolated prompt photon cross section in pp
collisions at $\sqrt{s}$ = 7 TeV with the ATLAS detector*, Phys. Rev. D **83** (2011) 052005,
arXiv: 1012.4389 [hep-ex].

[39] M. Cacciari, G. P. Salam, and G. Soyez, *The Catchment Area of Jets*, JHEP **04** (2008) 005,
arXiv: 0802.1188 [hep-ph].

[40] M. Cacciari, G. P. Salam, and S. Sapeta, *On the characterisation of the underlying event*,
JHEP **04** (2010) 065, arXiv: 0912.4926 [hep-ph].

[41] ATLAS Collaboration, *Measurement of isolated-photon pair production in pp collisions at
$\sqrt{s}$ = 7 TeV with the ATLAS detector*, JHEP **01** (2013) 086, arXiv: 1211.1913 [hep-ex].

[42] M. Oreglia, "A Study of the Reactions $\psi' \rightarrow \gamma\gamma\psi$," PhD thesis: SLAC, 1980,
URL: http://www.slac.stanford.edu/pubs/slacreports/slac-r-236.html.

[43] ATLAS Collaboration,
Search for resonances in diphoton events at $\sqrt{s}$ = 13 TeV with the ATLAS detector,
JHEP **09** (2016) 001, arXiv: 1606.03833 [hep-ex].

[44] ATLAS Collaboration, *Measurements of Higgs boson properties in the diphoton decay channel
with 36 fb^{-1} of pp collision data at $\sqrt{s}$ = 13 TeV with the ATLAS detector*, (2018),
arXiv: 1802.04146 [hep-ex].

[45] L. Devroye, *Sample-based Non-uniform Random Variate Generation*, WSC '86 (1986) 260,
URL: http://doi.acm.org/10.1145/318242.318443.

[46] G. Cowan, K. Cranmer, E. Gross, and O. Vitells,
      Asymptotic formulae for likelihood-based tests of new physics,
      Eur. Phys. J. **C71** (2011) 1554, [Erratum: Eur. Phys. J.C73,2501(2013)],
      arXiv: `1007.1727 [physics.data-an]`.

[47] A. L. Read, *Presentation of search results: The CL(s) technique*,
      J. Phys. **G28** (2002) 2693, [,11(2002)].